Mobile Rayleigh Doppler lidar for wind and temperature measurements in the stratosphere and lower mesosphere

Xiankang Dou,[1,2,*] Yuli Han,[1] Dongsong Sun,[1,2] Haiyun Xia,[1,2] Zhifeng Shu,[1,2] Ruocan Zhao,[1] Mingjia Shangguan,[1] and Jie Guo[1]

[1]*CAS Key Laboratory of Geospace Environment, Department of Geophysics and Planetary Sciences, University of Science and Technology of China, Hefei, 230026, China*

[2]*Mengcheng National Geophysical Observatory, School of Earth and Space Sciences, University of Science and Technology of China, Hefei, 230026, China*

[*]*dou@ustc.edu.cn*

Abstract: A mobile Rayleigh Doppler lidar based on the molecular double-edge technique is developed for measuring wind velocity in the middle atmosphere up to 60 km. The lidar uses three lasers with a mean power of 17.5 W at 355 nm each and three 1 m diameter telescopes to receive the backscattered echo: one points to zenith for vertical wind component and temperature measurement; the two others pointing toward east and north are titled at 30° from the zenith for zonal and meridional wind component, respectively. The Doppler shift of the backscattered echo is measured by inter-comparing the signal detected through each of the double-edge channels of a triple Fabry-Perot interferometer (FPI) tuned to either side of the emitted laser line. The third channel of FPI is used for frequency locking and a locking accuracy of 1.8 MHz RMS (root-mean-square) at 355 nm over 2 hours is realized, corresponding to a systematic error of 0.32 m/s. In this paper, we present detailed technical evolutions on system calibration. To validate the performance of the lidar, comparison experiments was carried out in December 2013, which showed good agreement with radiosondes but notable biases with ECMWF (European Centre for Medium range Weather Forecasts) in the height range of overlapping data. Wind observation over one month performed in Delhi (37.371° N, 97.374° E), northwest of China, demonstrated the stability and robustness of the system.

OCIS codes: (010.0010) Atmospheric and oceanic optics; (120.0280) Remote sensing and sensors; (280.3340) Laser Doppler velocimetry; (280.3640) Lidar.

References and links

1. J. W. Meriwether and A. J. Gerrard, "Mesosphere inversion layers and stratosphere temperature enhancements," Rev. Geophys. **42**(3), RG3003 (2004).
2. A. Müllemann and F. J. Lübken, "Horizontal winds in the mesosphere at high latitudes," Adv. Space Res. **35**(11), 1890–1894 (2005).
3. A. Hertzog, P. Cocquerez, C. Basdevant, G. Boccara, J. Bordereau, B. Brioit, A. Cardonne, R. Guilbon, A. Ravissot, É. Schmitt, J. N. Valdivia, S. Venel, and F. Vial, "Stratéole/vorcore-long-duration, superpressure balloons to study the Antarctic lower stratosphere during the 2005 winter," J. Atmos. Ocean. Technol. **24**(12), 2048–2061 (2007).
4. P. Hays, M. Dehring, L. Fisk, P. Tchoryk, I. Dors, J. Ryan, J. Wang, M. Hardesty, B. Gentry, and F. Hovis, "Space-based Doppler winds lidar: a vital national need," In response to national research council (NRC) decadal study request for information (RFI), May (2005).
5. European Space Agency ESA, *ADM-Aeolus science report: ESA SP-1311* (ESA Communication Production Office, 2008).
6. A. Stoffelen, J. Pailleux, E. Källen, J. M. Vaughan, L. Isaksen, P. Flamant, W. Wergen, E. Andersson, H. Schyberg, A. Culoma, R. Meynart, M. Endemann, and P. Ingmann, "The atmospheric dynamics mission for

#210185 - $15.00 USD Received 18 Apr 2014; revised 24 Jun 2014; accepted 25 Jun 2014; published 8 Jul 2014

global wind field measurement," Bull. Am. Meteorol. Soc. **86**(1), 73–87 (2005).
7. O. Reitebuch, C. Lemmerz, E. Nagel, U. Paffrath, Y. Durand, M. Endemann, F. Fabre, and M. Chaloupy, "The airborne demonstrator for the direct-detection Doppler wind lidar ALADIN on ADM-Aeolus. Part I: Instrument design and comparison to satellite instrument," J. Atmos. Ocean. Technol. **26**(12), 2501–2515 (2009).
8. U. Paffrath, C. Lemmerz, O. Reitebuch, B. Witschas, I. Nikolaus, and V. Freudenthaler, "The airborne demonstrator for the direct-detection Doppler wind lidar ALADIN on ADM-Aeolus. Part II: Simulations and Rayleigh Receiver Radiometric performance," J. Atmos. Ocean. Technol. **26**(12), 2516–2530 (2009).
9. M. L. Chanin, A. Garnier, A. Hauchecorne, and J. Porteneuve, "A Doppler lidar for measuring winds in the middle atmosphere," Geophys. Res. Lett. **16**(11), 1273–1276 (1989).
10. A. Garnier and M. L. Chanin, "Description of a Doppler Rayleigh lidar for measuring winds in the middle atmosphere," Appl. Phys. B **55**(1), 35–40 (1992).
11. C. Souprayen, A. Garnier, A. Hertzog, A. Hauchecorne, and J. Porteneuve, "Rayleigh-Mie Doppler wind lidar for atmospheric measurements. I. Instrumental setup, validation, and first climatological results," Appl. Opt. **38**(12), 2410–2421 (1999).
12. C. Souprayen, A. Garnier, and A. Hertzog, "Rayleigh-Mie Doppler wind lidar for atmospheric measurements. II. Mie scattering effect, theory, and calibration," Appl. Opt. **38**(12), 2422–2431 (1999).
13. C. A. Tepley, S. I. Sargoytchev, and C. O. Hines, "Initial Doppler Rayleigh lidar results from Arecibo," Geophys. Res. Lett. **18**(2), 167–170 (1991).
14. C. A. Tepley, S. I. Sargoytchev, and R. Rojas, "The Doppler Rayleigh lidar system at Arecibo," IEEE Trans. Geosci. Remote Sens. **31**(1), 36–47 (1993).
15. C. A. Tepley, "Neutral winds of the middle atmosphere observed at Arecibo using a Doppler Rayleigh lidar," J. Geophys. Res. **99**(D12), 25781–25790 (1994).
16. J. S. Friedman, C. A. Tepley, P. A. Castleberg, and H. Roe, "Middle-atmospheric Doppler lidar using an iodine-vapor edge filter," Opt. Lett. **22**(21), 1648–1650 (1997).
17. D. Rees, M. Vyssogorets, N. P. Meredith, E. Griffin, and Y. Chaxell, "The Doppler wind and temperature system of the ALOMAR lidar facility: overview and initial results," J. Atmos. Sol. Terr. Phys. **58**(16), 1827–1842 (1996).
18. U. von Zahn, G. von Cossart, J. Fiedler, K. H. Fricke, G. Nelke, G. Baumgarten, D. Rees, A. Hauchecorne, and K. Adolfsen, "The ALOMAR Rayleigh/Mie/Raman lidar: Objectives, configuration, and performance," Ann. Geophys. **18**(7), 815–833 (2000).
19. G. Baumgarten, "Doppler Rayleigh Mie Raman lidar for wind and temperature measurements in the middle atmosphere up to 80 km," Atmos. Meas. Tech. **3**(6), 1509–1518 (2010).
20. W. Huang, X. Chu, J. Wiig, B. Tan, C. Yamashita, T. Yuan, J. Yue, S. D. Harrell, C.-Y. She, B. P. Williams, J. S. Friedman, and R. M. Hardesty, "Field demonstration of simultaneous wind and temperature measurements from 5 to 50 km with a Na double-edge magneto-optic filter in a multi-frequency Doppler lidar," Opt. Lett. **34**(10), 1552–1554 (2009).
21. B. M. Gentry, H. Chen, and S. X. Li, "Wind measurements with 355-nm molecular Doppler lidar," Opt. Lett. **25**(17), 1231–1233 (2000).
22. F. Shen, H. H. Cha, J. Dong, D. Kim, D. Sun, and S. O. Kwon, "Design and performance simulation of a molecular Doppler wind lidar," Chin. Opt. Lett. **7**(7), 593–597 (2009).
23. H. Xia, X. Dou, D. Sun, Z. Shu, X. Xue, Y. Han, D. Hu, Y. L. Han, and T. Cheng, "Mid-altitude wind measurements with mobile Rayleigh Doppler lidar incorporating system-level optical frequency control method," Opt. Express **20**(14), 15286–15300 (2012).
24. Y. L. Han, X. Dou, D. Sun, H. Xia, Z. Shu, Y. Han, X. Xue, and T. Cheng, "Analysis on wind retrieval methods for Rayleigh Doppler lidar," Opt. Eng. **53**(6), 061607 (2014).
25. Z. Shu, Z. Shu, H. Xia, D. Sun, Y. Han, C. Hyunki, K. Dukhyeon, G. Wang, B. Sunghoon, and D. Hu, "Low stratospheric wind measurement using mobile Rayleigh Doppler Wind LIDAR," J. Opt. Soc. Korea. **16**(2), 141–144 (2012).
26. H. Xia, D. Sun, Y. Yang, F. Shen, J. Dong, and T. Kobayashi, "Fabry-Perot interferometer based Mie Doppler lidar for low tropospheric wind observation," Appl. Opt. **46**(29), 7120–7131 (2007).
27. C. L. Korb, B. M. Gentry, S. X. Li, and C. Flesia, "Theory of the double-edge technique for Doppler lidar wind measurement," Appl. Opt. **37**(15), 3097–3104 (1998).
28. C. Flesia and C. L. Korb, "Theory of the double-edge molecular technique for Doppler lidar wind measurement," Appl. Opt. **38**(3), 432–440 (1999).
29. Z. S. Liu, D. Wu, J. T. Liu, K. L. Zhang, W. B. Chen, X. Q. Song, J. W. Hair, and C. Y. She, "Low-altitude atmospheric wind measurement from the combined Mie and Rayleigh backscattering by Doppler lidar with an iodine filter," Appl. Opt. **41**(33), 7079–7086 (2002).
30. J. A. McKay, "Assessment of a multibeam Fizeau wedge interferometer for Doppler wind lidar," Appl. Opt. **41**(9), 1760–1767 (2002).
31. D. Bruneau, A. Garnier, A. Hertzog, and J. Porteneuve, "Wind-velocity lidar measurements by use of a Mach-Zehnder interferometer, comparison with a Fabry-Perot interferometer," Appl. Opt. **43**(1), 173–182 (2004).
32. N. Cézard, A. Dolfi-Bouteyre, J. P. Huignard, and P. H. Flamant, "Performance evaluation of a dual fringe-imaging Michelson interferometer for air parameter measurements with a 355 nm Rayleigh-Mie lidar," Appl. Opt. **48**(12), 2321–2332 (2009).
33. C. Weitkamp, *Range-Resolved Optical Remote Sensing of the Atmosphere* (Springer, 2005), pp. 273–281.

#210185 - $15.00 USD Received 18 Apr 2014; revised 24 Jun 2014; accepted 25 Jun 2014; published 8 Jul 2014

34. A. Hauchecorne, M. L. Chanin, and P. Keckhut, "Climatology and trends of the middle atmospheric temperature (33–87 km) as seen by Rayleigh lidar over the south of France," J. Geophys. Res. **96**(D8), 15297–15309 (1991).
35. V. Ramaswamy, M. L. Chanin, J. Angell, J. Barnett, D. Gaffen, M. Gelman, P. Keckhut, Y. Koshelkov, J. Labitzke, J. R. Lin, A. O'Neill, J. Nash, W. Randel, R. Rood, K. Shine, M. Shiotani, and R. Swinbank, "Stratospheric temperature trends: Observations and model simulations," Rev. Geophys. **39**(1), 71–122 (2001).
36. J. A. McKay, "Modeling of direct detection Doppler wind lidar. I. The edge technique," Appl. Opt. **37**(27), 6480–6486 (1998).
37. J. A. McKay, "Modeling of direct detection Doppler wind lidar. II. The fringe imaging technique," Appl. Opt. **37**(27), 6487–6493 (1998).
38. J. A. McKay, "Comment on "Theory of the double-edge molecular technique for Doppler lidar wind measurement"," Appl. Opt. **39**(6), 993–996 (2000).
39. O. Reitebuch, C. Lemmerz, U. Marksteiner, S. Rahm, and B. Witschas, "Airborne lidar observations supporting the ADM-Aeolus mission for global wind profiling," in *26th Int. Laser Radar Conference*, Porto Heli, Greece (2012), S5O-01.
40. B. Witschas, C. Lemmerz, and O. Reitebuch, "Horizontal LIDAR measurements for the proof of spontaneous Rayleigh-Brillouin scattering in the atmosphere," Appl. Opt. **51**(25), 6207–6219 (2012).
41. B. Witschas, "Analytical model for Rayleigh-Brillouin line shapes in air," Appl. Opt. **50**(3), 267–270 (2011).
42. R. G. Seasholtz, "2D velocity and temperature measurements in high speed flows based on spectrally resolved Rayleigh scattering," in *New Trends in Instrumentation for Hypersonic Research*, Vol. 224 of NATO ASI Series (Springer, 1993), pp. 399–408.
43. A. Dabas, M. L. Denneulin, P. Flamant, C. Loth, A. Garnier, and A. Dolfi-Bouteyre, "Correcting winds measured with a Rayleigh Doppler lidar from pressure and temperature effects," Tellus, Ser. A, Dyn. Meterol. Oceanogr. **60**(2), 206–215 (2008).
44. M. J. McGill, W. R. Skinner, and T. D. Irgang, "Analysis techniques for the recovery of winds and backscatter coefficients from a multiple-channel incoherent Doppler lidar," Appl. Opt. **36**(6), 1253–1268 (1997).
45. T. Schröder, C. Lemmerz, O. Reitebuch, M. Wirth, C. Wührer, and R. Treichel, "Frequency jitter and spectral width of an injection-seeded Q-switched Nd:YAG laser for a Doppler wind lidar," Appl. Phys. B **87**(3), 437–444 (2007).
46. B. M. Knudsen, J. M. Rosen, N. T. Kjome, and A. T. Whitten, "Comparison of analyzed stratospheric temperatures and calculated trajectories with long-duration balloon data," J. Geophys. Res. **101**(D14), 19137–19145 (1996).
47. A. D. Belmont, D. G. Dartt, and G. D. Nastrom, "Variations of stratospheric zonal winds, 20-65 km, 1961-1971," J. Appl. Meteorol. **14**(4), 585–594 (1975).
48. T. Li, X. Fang, W. Liu, S. Y. Gu, and X. Dou, "Narrowband sodium lidar for the measurements of mesopause region temperature and wind," Appl. Opt. **51**(22), 5401–5411 (2012).

1. Introduction

Wind and temperature measurement are fundamental for a comprehensive understanding of atmospheric dynamics on small (<100 km) to global scales. In spite of numerous instrumental developments contributes to a better description of the middle atmosphere both from ground and satellites, wind measurement in the altitude range 15-60 km is still poorly reported [1, 6]. Such altitude, where most time the aerosol contribution is negligible, is too high for conventional balloons sounding (generally below 40 km) and is located below the ionosphere, as a result, radars cannot receive significant backscatter for determining winds. Rockets cover this region but only allow sporadic soundings and cannot fulfill the time/altitude cross section of temperatures and winds [2]. Recent report proved that superpressure balloons can reliably perform long-duration flights in very harsh environment, which enriches the observation techniques for stratospheric wind and temperature [3]. The space-borne Doppler Wind Lidar (DWL) is now regards as the most promising candidate to achieve a coverage of global wind measurements. In the Atmospheric Dynamics Mission Aeolus (ADM-Aeolus) payload Atmospheric Laser Doppler Instrument (ALADIN), which has been demonstrated by airborne validation and scheduled to be launched in the near future, observation of stratospheric wind profiles is merely expected to be 30 km altitude [4–8].

Until now, the interpretation of most middle atmospheric dynamical data relies on the climatological description of wind field and various atmospheric models. Numerous theories exist to describe the interaction between the waves and the general circulation. However, a full understanding of the process and meaningful verification of these theories require simultaneous observations of the wind field fluctuations. Furthermore, the detection of sharp wind shears, which often encountered at the stratopause and play an important role in

#210185 - $15.00 USD Received 18 Apr 2014; revised 24 Jun 2014; accepted 25 Jun 2014; published 8 Jul 2014

reflecting or filtering the waves, need very high vertical resolution (~1 km). Such height resolution is inaccessible to satellite instruments. Therefore the ground-based Rayleigh Doppler lidar is the only remote sensing instrument in the stratosphere and lower mesosphere in the foreseeable future.

Although the possibility to measurement winds in the middle atmosphere with a Doppler lidar has already been demonstrated more than two decades ago, there are only few reports of stratospheric wind measurements with direct-detection Rayleigh Doppler lidars. Wind measurement in the stratosphere up to 50 km altitude was firstly realized by Chanin *et al.* using two high resolution and narrow bandpass Fabry-Perot interferometers as frequency discriminator at the Observatory of Haute Provence (OHP), France [9–12]. Tepley *et al.* developed another technique for wind measurement up to an altitude near 60 km, in which a single FPI was used for spectral scanning of the Rayleigh backscattered spectrum [13–16]. At the ALOMAR research station in Northern Norway, a Rayleigh/Mie/Raman lidar combined FPI and a Doppler Rayleigh Iodine Spectrometer was implemented for simultaneous wind and temperature detection in the stratosphere and mesosphere up to 80 km [17–19]. Recent report revealed a direct detection system working at 589 nm with a sodium filter was developed to cover the altitude range from 10 km to 45 km at Fort Collins, Colorado [20]. In order to take advantage of the λ^{-4} dependence of the Rayleigh backscattering, the Goddard Lidar Observatory for Winds (GLOW) mobile Doppler lidar choose a frequency tripled Nd:YAG laser working at 355 nm with a double-edge FPI for stratosphere wind measurement at NASA Goddard Space Flight Center [21]. A similar mobile Rayleigh Doppler wind lidar was implemented and demonstrated capable to measure quasi-simultaneous wind from upper troposphere to stratosphere (8~40 km) at University of Science and Technology of China (USTC) [22–26].

Recently, based on the prototype setup, we developed another mobile Rayleigh Doppler lidar system for simultaneous stratospheric and lower mesospheric wind and temperature measurement up to 60 km. In this paper we describe the detailed system setup and present the observation results performed at Delhi (37.371° N, 97.374° E), northwest of China. The lidar measurements are compared with radiosonde wind measurements taken simultaneously at the same location and ECMWF.

2. Description of the method

The direct-detection technique has been developed to extend the wind measurement capability into the troposphere and stratosphere by using various high resolution frequency discriminators, such as Fabry-Perot Interferometers [27,28], iodine absorption [29], Fizzeau interferometer [30], Mach-Zehnder interferometer [31] and Michelson interferometer [32]. In this work, a triple channel FPI, which is capacitively stabilized and piezo-electrically tunable, is utilized as frequency discriminator to determine the wind velocity with its double-edge channels located in the wings of the thermally broadened molecular backscattered signal spectrum. The frequency of outgoing laser is locked at the cross-point of the double-edge channels by scanning the cavity length of the FPI and is monitored by measuring the transmission changes of the outgoing laser on the locking channel to remove the inaccuracies due to the frequency drift of the laser and FPI. Because of the symmetric arrangement of the FPI about the laser frequency, the Doppler shift will cause the transmitted signal to increase in one edge channel and to decrease in the other one. In a certain line of sight (LOS), we calculate the response *R(z)* at each altitude z, defined as

$$R(z) = \frac{CN_1(z) - N_2(z)}{CN_1(z) + N_2(z)}. \tag{1}$$

Where $N_1(z)$ and $N_2(z)$ are the numbers of photons from altitude z transmitted through edge 1 and 2 channel, respectively; C is a corrective factor introduced to account for the possible

#210185 - $15.00 USD Received 18 Apr 2014; revised 24 Jun 2014; accepted 25 Jun 2014; published 8 Jul 2014

imbalance between the double-edge channels. The response profile *R(z)*, representative of backscatter line position with respect to the FPI bandpasses, is sensitive to the wind velocity and provides a unique measure of it. One can deduce the Doppler shift profile $\Delta v_d(z)$ from the response profile *R(z)* through the instrumental calibration function by accounting for the atmospheric temperature profile. Each wind component along LOS is calculated as follows:

$$V_h(z) = \frac{\lambda}{2\sin\theta}\Delta v_d(z) \tag{2}$$

Where θ is the zenith angle of the telescope and λ is the emitted wavelength (355nm). In this system, three 1 m diameter telescopes are configured for wind measurement: one points to zenith and the two others with eastward and northward pointing are titled at 30° from the zenith. Therefore, the wind vector is resultant of three components with different pointing directions, as shown in Fig. 1.

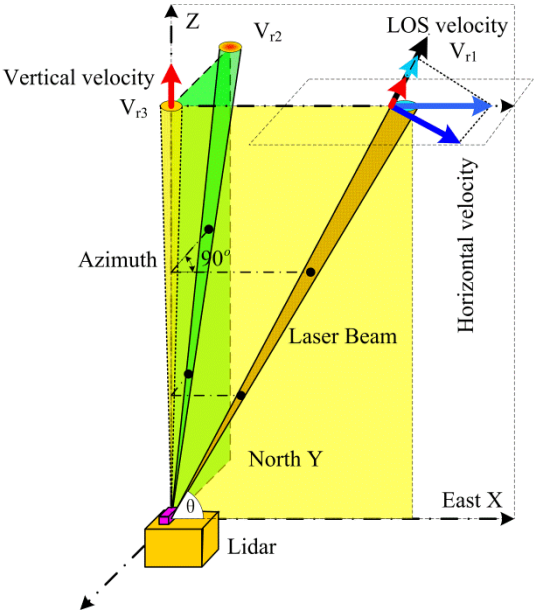

Fig. 1. Schematic view of the lidar receiver setup. Three cones are drawn for the eastward, northward and vertical pointing. The east and north pointing are at an angle of 30° from the zenith. The vertical and horizontal components of wind vector are determined by them, as shown in this figure.

Besides vertical component of wind measurements, the vertical backscatter is also used to calculate simultaneously temperature. Today, lidar techniques for the remote sensing of atmospheric temperature profiles have reached the maturity necessary for routine observations [33–35]. In this work, we utilize the integration technique with a molecular backscatter signal to determine the atmospheric temperature. The intensity of a molecular lidar signal is proportional to the number density of the atmospheric molecules at a certain altitude. Under the assumption that the atmosphere is in hydrostatic equilibrium and with the initialization at a reference altitude, the temperature profile can be derived from the ideal-gas law by accounting for the number density profile.

Generally, atmospheric backscatter consist of two components: Rayleigh and Mie with different spectral widths and in a ratio that is highly variable with altitude and atmospheric conditions. This difference in spectral widths has little effect on the calibration of a fringe imaging Doppler analyzer designed for Rayleigh backscatter, because the displacement of the Fabry-Perot maximum versus frequency shift is independent of the signal spectral width

#210185 - $15.00 USD Received 18 Apr 2014; revised 24 Jun 2014; accepted 25 Jun 2014; published 8 Jul 2014

[36,37]. While for the edge technique or its variation, the double-edge technique, this effect is profound because the calibration of amplitude change versus frequency shift decreases with increasing spectral width. In this work, the altitude range we aim to cover with our new generation Doppler lidar is the entire stratosphere and lower mesosphere from 15 km up to 60 km. Within this height range, the contribution of aerosol was traditionally thought to be very weak in most situations and could be negligible when compared with other error sources in the measurements. However, this cognition ceased to exist after volcanic eruption injected large quantities of aerosol into the stratosphere, preventing reliable wind observations with Rayleigh backscatter, double-edge systems. To solve this problem, the CNRS (the Centre National de la Recherche Scientifique) group and the GLOW group gave their own implementations of double-edge technique that greatly reduce the contamination of Mie component in the Rayleigh signal [9, 28]. Later, Mckay demonstrated that their experimentally validated solutions were theoretically coincident with each other [38]. Likewise, a specific focus in our system is given on optimizing the characteristics of the FPI and the related impact of Mie scattering by numerical simulations, as depicted in Fig. 2.

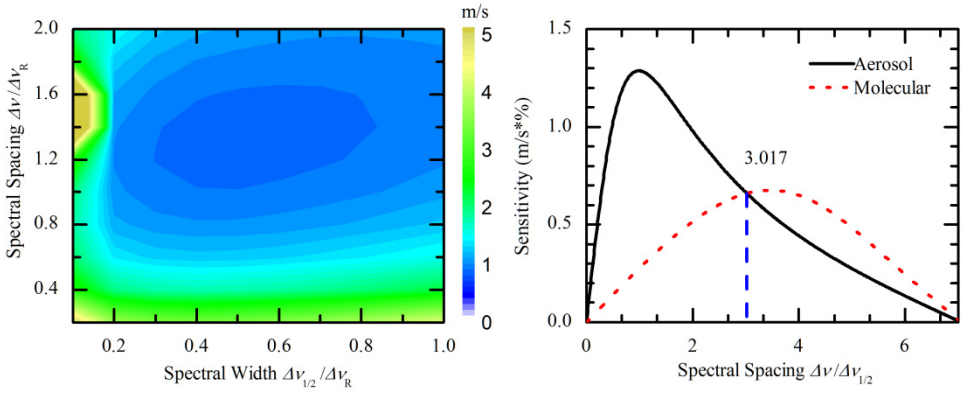

Fig. 2. (a) Evolution of the wind velocity error versus the full width at half maximum (FWHM) of FPI bandpasses and spectral spacing between the double-edge channels (in units of Rayleigh spectrum width $\Delta\nu_R$ at 226.5 K). (b) The Doppler sensitivity, i.e., percentage change in the normalized signal for a velocity of 1 m/s, plotted as a function of spectral spacing (in unit of FWHM of the FPI). T = 226.5 K.

Two parameters, the full width at half maximum (FWHM) of each FPI channel $\Delta\nu_{1/2}$ and the spectral spacing between the double-edge channels $\Delta\nu$ are chosen to minimize the statistical standard error on the wind velocity. Based on the double-edge theory [27, 28], the error in line-of-sight wind is given as

$$\varepsilon = \frac{1}{\Theta \cdot SNR}, \tag{3}$$

where Θ is the measurement sensitivity and *SNR* is the signal to noise ratio for double edge measurement. The measurement sensitivity Θ is calculated by the FWHM related FPI transmission curve, whereas the *SNR* is obtained from numerical simulation on a basis of lidar equation, which takes the counting uncertainties, Mie scattering pollution and detector noises into accounts. Generally, the measurement sensitivity increases as the FWHM of FPI decreases. However, the narrower the FWHM of FPI, the fewer the transmitted photons, which yields a lower *SNR*. A similar contradictory relationship exists in the spectral spacing, which greatly affects the Mie sensitivity and its contribution to the *SNR*. As there is no correlation between the Mie effect and the spectral characteristic of the locking channel, thus

#210185 - $15.00 USD Received 18 Apr 2014; revised 24 Jun 2014; accepted 25 Jun 2014; published 8 Jul 2014

is not considered in the simulation procedure. The simulations are performed for an atmospheric temperature of 226.5 K. Figure 2(a) shows the evolution of the wind velocity error versus the FWHM of FPI and spectral spacing between the double-edge channels in unit of Rayleigh spectrum width at 226.5 K (~3.38 GHz). The result reveals that the smallest error happens at spectral spacing of 1.2~1.4 $\Delta\nu_R$ (4.06~4.74 GHz) and the FWHM of FPI of 0.5~0.6 $\Delta\nu_R$ (1.69~2.03 GHz). In Fig. 2(b), the velocity sensitivity for both molecular and aerosol backscattering is reported as a function of spectral spacing in unit of FWHM of FPI. In order to make the measurement insensitive to Mie scattering, the spectral spacing required to be at the crossover region (3.017 $\Delta\nu_{1/2}$). Considering the middle atmospheric conditions (200~280 K), the spectral characteristics was finally selected to be: $\Delta\nu_{1/2}$ = 1.7 GHz and $\Delta\nu$ = 5.1 GHz.

3. Instrumental setup

The USTC Rayleigh Doppler lidar system includes three independent subsystems: one points to the zenith for vertical wind component and temperature measurement as well as null Doppler-shift calibration; the two others are tilted at 30° from the zenith with eastward and northward pointing for meridional and zonal wind components, respectively. The different subsystems have nearly identical optical properties with slightly different in temperature detection module incorporated in the vertical subsystem. Therefore, each could realize line of sight (LOS) wind detection independently. Three dimensional wind field are obtained simultaneously from resultant of them. As an example, Fig. 3 gives the schematic view of the optical setup for the vertical subsystem.

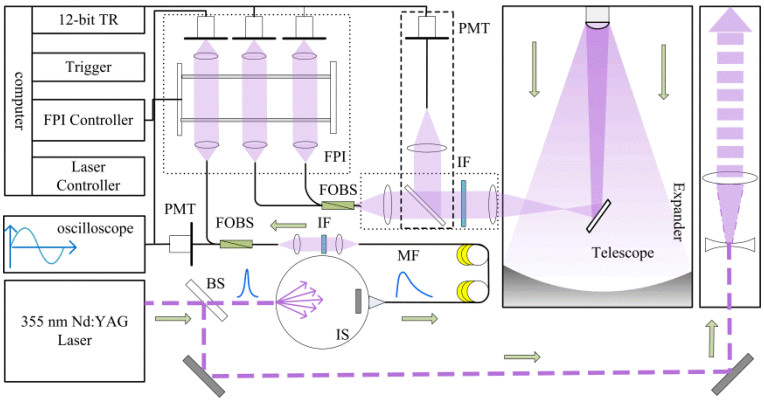

Fig. 3. Schematic view of the lidar optical setup: BS, beam splitter; IS, integrating sphere, MF, multimode fiber; FOBS, fiber-optic beam splitter; PMT, photomultiplier tube; FPI, Fabry-Perot interferometer; TR, transient recorder.

This system adopts a Q-switched, flash-pumped and frequency tripled Nd:YAG laser (Continuum Model Powerlite 9050) working at 355 nm, made stable master frequency in the slave cavity and single longitudinal mode by the injection of a very narrow linewidth fiber laser (Continuum SI-2000, linewidth < 5 KHz). To achieve a high stability, the seed laser is in continuous operation and is thermally controlled (± 0.1 K) to ensure long-time operation of the injection. The pulse repetition rate is 50 Hz and the energy per pulse at the tripled wavelength of 355 nm is approximately 350 mJ. The emitted spectral line shape can be represented by a Gaussian distribution with spectral width of about 200 MHz, much smaller than the spectral width of either the atmospheric signal (~3.5 GHz) or the double-edge interferometers (1.7 GHz). A very small fraction of the outgoing laser beam transmitted through a 0.25m diameter integrating sphere is used as a feedback signal to actively lock the

#210185 - $15.00 USD Received 18 Apr 2014; revised 24 Jun 2014; accepted 25 Jun 2014; published 8 Jul 2014

frequency of the emitted laser to the crosspoint of the double-edge channels' transmission curve. The pulsed reference signal, stretched by the integrating sphere from ~7 ns to ~25 ns in time domain, is accurately sampled by an oscilloscope (2.5 GS/s), which ensures a high signal to noise ratio (SNR) for the locking procedure. The elastic backscatter from air molecules and possibly other particles is received by a Cassegrain telescope with 1 m in diameter and 0.09 mrad in field of view (FOV). To each of the receive telescope corresponds an afocal transmitter, which compress divergence of the laser beam from 0.5 mrad to about 0.04 mrad aiming to eliminate the sky background as far as possible. To avoid saturation of the detectors at short ranges, the range-gating electronics synchronized with the laser pulse emission is utilized to block the atmospheric signal by a variable time of usually 40 μs, corresponding vertical altitude of 6 km. A 200 μm diameter multimode fiber (MF) is placed at the focus of the telescope to guide the collected signal to the PFI for wind determination. The FPI is set in a thermally controlled container insures for all channels of the FPI exactly the same spectral stability. The signal pass through the FPI is focused onto a photomultiplier tube (PMT) and sampled by a 12-bit transient recorder (TR), which contains 2 preamplifiers optimized for high linearity for analog detection and for maximum speed and gain for photon counting. A narrow bandpass interferometer filter at 355 nm with FWHM of 0.15 nm is used to suppress the background for daytime operation. The laser operation, FPI spacing/parallelism, as well as transient recorder and oscilloscope sampling are controlled by an industrial computer via RS232 interfaces or Ethernet with software developed to accomplish real-time signal processing and unattended operation. The system parameters are summarized in Table 1.

Table 1. Key parameters of the mobile Rayleigh Doppler Lidar

Parameter		Value
Transmitter		
	Wavelength (nm)	355
	Laser 1/e width (MHz)	200
	Laser energy/pulse (mJ)	350
	Laser repetition rate (Hz)	50
Transceiver		
	Telescope aperture (m)	1
	Field of view (mrad)	0.09
	Zenith angle (°)	30 or 0
	Optical efficiency (%)	85
Receiver		
	FSR (GHz)	12
	FWHM (GHz)	1.7
	Edge channel separation (GHz)	5.1
	Peak transmission (%)	60
	PMT Quantum Efficiency (%)	21

To simply the instrument system setup, we use one single polychromatic front optical system by coupling the backscatter collected from the telescope alternatingly into the wind and temperature measurement system, as depicted in the dashed box in Fig. 3. The reflecting mirror is motivated by a stepper motor: for wind measurement, it will be removed, then the collimated light is focused into an MF and split into two beams by fiber-optic beam splitter (FOBS) for Doppler shift detections; while for temperature measurement, the collimated light will be directly focused into a MF and coupled onto a PMT. Assuming hydrostatic equilibrium, the simultaneously atmospheric height profile of temperature can be obtained through integration by accounting for the relative density profile.

As mentioned above, the altitude range we aim to cover in this work is the stratosphere and lower mesosphere, which requires the detector working at photon counting mode has sufficient dynamic range to cover such altitude range. This is full of challenges for most photoelectric detectors. The Rayleigh/Mie/Raman lidar implemented in ALOMAR conceived and demonstrated an effective solution which uses a Doppler Rayleigh Iodine Spectrometer (DoRIS) with two branches of intensity cascaded channels to cover the dynamic range from

#210185 - $15.00 USD Received 18 Apr 2014; revised 24 Jun 2014; accepted 25 Jun 2014; published 8 Jul 2014

10 to 100 km altitude for simultaneous wind and temperature observation, however, it is not applicable to our ultraviolet system [19]. To deal with this problem, a compact design is performed by combining a stabilized dynode chain for strong light pulses with fast rise times (<1.3 ns) and narrow pulse widths (<2.2 ns) for high single photon count rates. This combination allows high dynamic range measurements by using both analog and photon counting measurements together, thus extending the linear dynamic range to 5 orders of magnitude. Additional advantages are reduced space charge effects and higher light levels that can be measured without suffering from nonlinearities, especially during the locking procedure. Triggered by a high level of transistor-transistor logic (TTL) from a programmable range-gating electronics, the detector is successfully employed to the data acquisition (DAQ). It is useful to step through the timing sequence for a single laser pulse to understand how the signals are collected, which is depicted in Fig. 4.

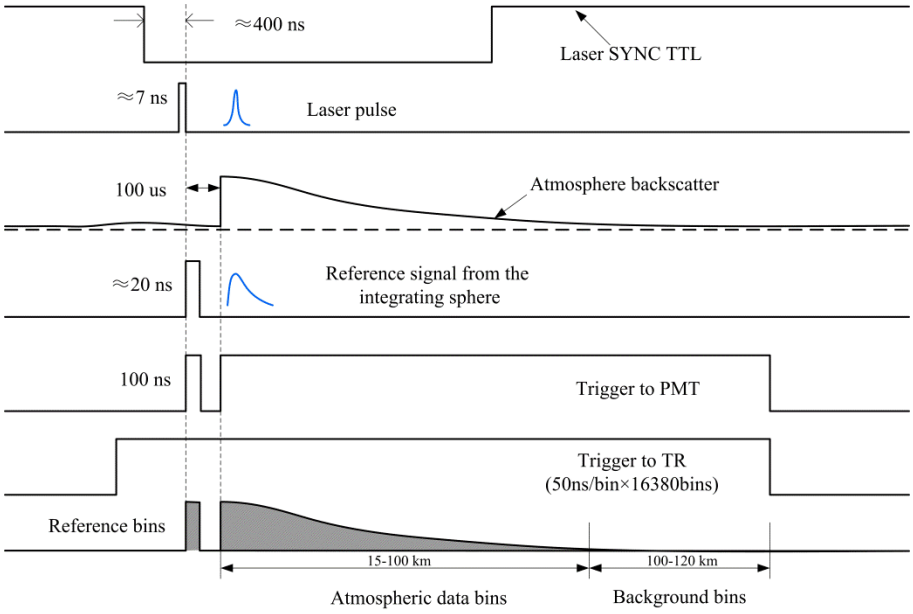

Fig. 4. Data acquisition timing sequence

The SYNC TTL signal from the laser was used to synchronize the range-gating electronics. The reference bins collected by the oscilloscope after the Q switch is used to measure the line position of emitted laser with respect to the transmission curve of FPI. In order to prevent the detector from saturation, the trigger generates a low level of transistor-transistor logic (TTL) output during the Q switch to the light spreading to the altitude of 6 km. The tail of atmosphere backscatter within the altitude range from 100 to 120 km is used as the average background. The final output data from the transient recorder is shown in Fig. 4.

4. Characterization of the system calibration

Two years ago, our realization of a mobile Rayleigh Doppler lidar is a system designed for quasi-simultaneous and routine soundings of wind field in the middle atmosphere with high stability. In a way, the quasi-simultaneous wind field is not a limitation for geophysical studies involving the sole vertical structure of the waves or mean shear etc.; nevertheless, it is not satisfactory for studies of smaller time scales of surface turbulence, wave transport and mixing, which contribute a lot to calculations of the atmospheric budget and general circulation. Furthermore, temperature profile as a necessary input parameter to many remote-sensing techniques including lidar for the determination of winds are under routine

#210185 - $15.00 USD Received 18 Apr 2014; revised 24 Jun 2014; accepted 25 Jun 2014; published 8 Jul 2014

observations in our new generation system. Some technique evolutions are introduced exhaustively in this section.

4.1 Frequency locking of emitted laser

The long-term frequency drift of the outgoing laser with respect to the FPI is controlled by a serve-loop acting on the FPI tuning control on a basis of accurate measurement of its transmission change on the FPI locking channel. For fiber coupling system, however, the different status of mode coupling within the guided fiber introduced variations in the angular distribution of the collimated beam to the FPI, and thus the transmission. In our prototype system, this problem is solved by using a mode scrambler optimized for 200 μm core with graded-index fibers mounted on the transfer optical fiber when detecting the transmitted laser frequency. It presses the fiber between specially designed corrugated surfaces to cause micro bending of the fiber so as to dramatically increase mode coupling among guided modes and coupling of high-order guided modes to radiation modes. The distribution of power among the modes is then independent of the coupling condition of the laser. Drawing inspiration but different from applications in the ADM-Aeolus, a 25 cm diameter integrating sphere instead of the mode scrambler is adopted for light coupling in the front optics of the FPI [7]. Integrating spheres are widely used in radiometric applications because of their superior performance in transforming radiation to a nearly ideal Lambertian distribution despite various conditions of the incident radiation. In this work, the integrating sphere is interiorly covered with $BaSO_4$, a diffuse white reflective coating with high reflectivity and chemical inertness. With an interferometer filter incorporated in the output port of the integrating sphere, it prevents the signal from pollution by potential fluorescence, which is of critical importance for spectrally analysis. The integrating sphere plays important roles on two aspects: on one hand, it stretches the laser pulse duration from ~7 ns to ~25 ns in time domain without broadening its spectra in frequency domain, leading to sufficient and accurate signal sampling; on the other hand, due to the uniform scattering property of the integrating sphere, the laser pulse passing through it and directed to the optical receiver by a multimode fiber allows uniform illumination on the FPI.

On the basis of integrating sphere theory, if rapidly varying light signals such as short pulses or those modulated at high frequencies are introduced into an integrating sphere, the output signal may be noticeably distorted by the “pulse stretching” caused by the multiple diffuse reflections. Experimental result of pulse stretching is represented in Fig. 5. As shown, the stretched pulse duration is about 2.5 times longer than the original pulse.

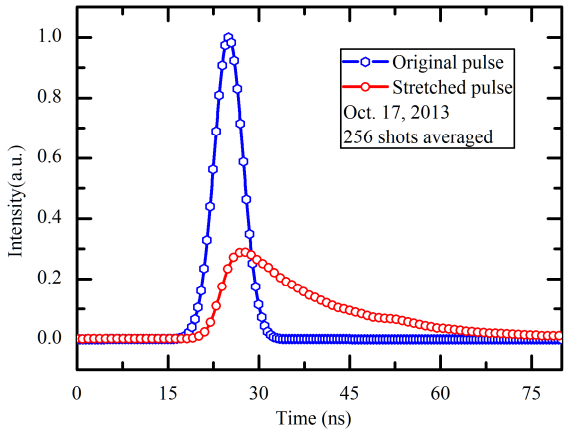

Fig. 5. Experimental result of integrating sphere stretching effect. The diameter of the integrating sphere used in this experiment is 25 cm. Both the input and exit port areas are 0.785 cm^2. The experimental result is a 256 shots average.

#210185 - $15.00 USD Received 18 Apr 2014; revised 24 Jun 2014; accepted 25 Jun 2014; published 8 Jul 2014

Stable and homogeneous patterns in the multimode fiber desired uniform irradiance. Integrating sphere features a radiance that is perfectly diffuse, independent of viewing angle. By butt coupling the multimode fiber to the output port of the integrating sphere, light collected from an area of the fiber core and an angle of numerical aperture (NA) shows perfect uniformity property. Two sets of typical experiments are shown in Fig. 6.

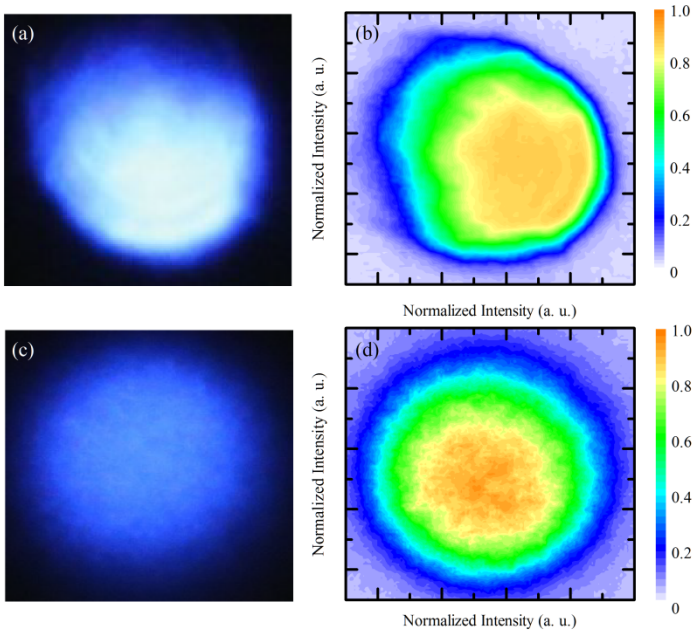

Fig. 6. Illumination patterns under the function of the integrating sphere. (a) is the output illumination pattern by directly coupled into an multimode fiber and (c) is its normalized intensity distribution; (c) is the output illumination pattern coupled from the integrating sphere and (d) is its normalized intensity.

The purpose of all our efforts is to improve the accuracy and stability of frequency locking for this system. Experiments to further validate the role of the integrating sphere are performed through daily morning and locking the frequency of the emitted laser. The experiments are carried out in a laboratory environment, with seeder and FPI thermally controlled. Figure 7(a) gives the variation of locked transmission and corresponding wind deviation. A locking accuracy of 1.8 MHz at 355 nm is realized, corresponding to a standard deviation error of 0.32 m/s in LOS wind velocity. Quasi-continuous operation for 11 days in October 2013 shows good stability. The locking accuracy of everyday tracking and mean deviation of wind velocity is represented in Fig. 7(b). One can see that the minimum and maximum deviation in this case is 0.23 m/s and 0.37 m/s, respectively.

#210185 - $15.00 USD Received 18 Apr 2014; revised 24 Jun 2014; accepted 25 Jun 2014; published 8 Jul 2014

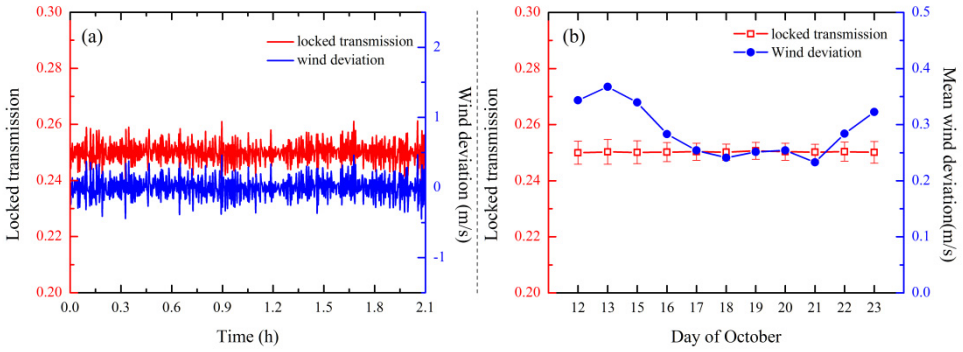

Fig. 7. Stability of the locked transmission and corresponding systemic error in LOS wind velocity. (a) presents the result of short-term tracking and simultaneous wind deviation over 2 hours on Oct. 12; (b) gives the long-term tracking for 11 days and mean statistics standard error in LOS wind velocity.

4.2 Null Doppler shift reference

A careful determination of null Doppler shift reference is necessary to get absolute winds measurements. In our prototype system, the response profile R(z) are deduced from theoretical calculation by accounting for spectral line shape of atmospheric backscatter and temperature profile at different altitudes. Considering the impact of temperature and pressure, the Tenti S6 model is considered to be the most appropriate line shape model to describe the spectrum of atmospheric backscatter in the retrieval algorithms, which was recently validated both in laboratory environment and in real atmosphere [39–43]. Note that the spectral line used to determine the wind velocity is broadened and shaped after interaction with the atmospheric constituents and that as close as possible, it should be calibrated by information coming from the actual response function with exact null Doppler shift reference rather than from a theoretical one. In this work, it is realized by scanning the FPI cavity length with vertical atmospheric backscatter for the double-edge channels and with a small portion of outgoing laser for the locking channel, respectively. For a FPI with a cavity length of 12.5 mm, 1 nm change in cavity length equates to 67.7 MHz in frequency Doppler shift or 12 m/s bias in LOS wind velocity at the working wavelength of 355 nm. Therefore, the dependence of Rayleigh response $R(z_0,v)$ versus wind velocity v is obtained through calculating Eq. (1) with the number of photons received from a certain altitude z_0 at every step of scanning. However, this approach is merely suitable to altitudes below 30 km due to the low *SNR* at high altitude. For altitude range from 30 km to 60 km, the number of photons in Eq. (1) is substituted with a theoretical Rayleigh transmission curve, which is the convolution of FPI edge function, laser spectrum, and the Tenti S6 model represented Rayleigh spectrum. During the scanning, the null Doppler shift reference, i.e. the zero wind velocity position, is determined by the crosspoint of the double-edge transmission curves scanned with 20 km to 25 km averaged backscatter, where quasi-zero wind layer was observed based on our original Rayleigh Doppler lidar [23]. The frequency of outgoing laser is locked at the null Doppler shift position throughout the wind detection, which ensures the system capable to make unbiased measurement after calibration. This adjustment, performed at the beginning of each night of measurements, revealed two major technique evolutions compared with our prototype setup. First, providing that the contribution of vertical velocity could be negligible (generally a few centimeters per second in the stratosphere), it gave a null Doppler-shift reference, which is of critical importance for non-scanning lidar system. In our prototype system, the lidar works in a step stare scanning mode at a fixed zenith angle of 30° with azimuths corresponding to four cardinal points. Therefore the systematic error in relation to uncalibrated zero-wind reference could be eliminated by differential measurements of two

#210185 - $15.00 USD Received 18 Apr 2014; revised 24 Jun 2014; accepted 25 Jun 2014; published 8 Jul 2014

opposite directions. However, the price is a lower temporal resolution and cannot fulfill the requirement of simultaneous observations of the wind field. Second, the Brillouin effect resulting from light scattering on spontaneous acoustic waves propagating in the atmosphere could be perceived in due time so as to remove its impact on wind determination. The fingerprint of Brillouin scattering on the spectral line shape is clearly identified from the lidar observation over a frequency of 16 GHz, as shown in Fig. 8. As an example, the backscatter from 6 km to 6.75 km (100 bins) is used. Owing to use a pure Gaussian approximation for atmospheric spectral line shape, the residual between the fitted transmission curve and lidar measurement shows a Brillouin doublet, which would cause a systematic error if being neglected in the wind retrieval algorithm.

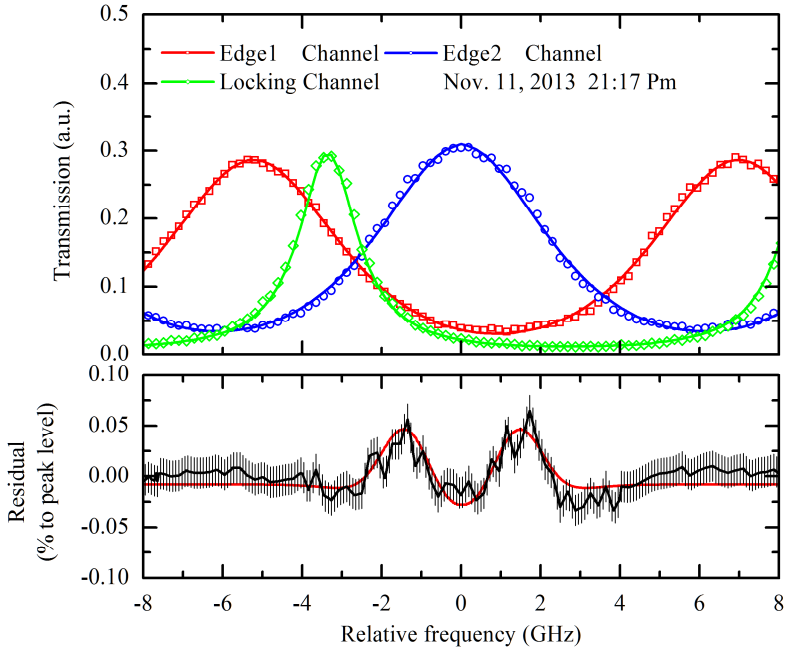

Fig. 8. (Top) Plotted actual atmospheric transmission curves with least-square fitted lines; The curve of locking channel is scanned by portion of the outgoing laser, while the two others are scanned by vertical backscatter from average of 6 km~6.75 km altitude, which are broaden by the random thermal motions of atmospheric particles. Each plot is 600 shots accumulated (~12 second) and the adjacent plots is changed in discrete frequency steps of about 190 MHz; (Bottom) Residual between measurement and fitted lines shape normalized to its peak level; the red line depict the fitting result with a set of Tenti S6 model line shapes subtract the central Gaussian line.

4.3 Calibration of instrumental drift

Middle atmospheric Doppler Rayleigh lidar wind measurements are usually performed with a single-mode pulsed laser transmitter and a Fabry-Perot interferometer on the receiver to discriminate frequency. Owning to thermal variation, Rayleigh Doppler lidars are suffering from instrumental drift. This drift profoundly manifested in the wind profiles, the characteristic feature of which is the almost identical vertical structure but with an overall bias on absolute value when compared to an ancillary data, such as radiosonde measurements. A residual difference of 5 m/s to 15 m/s between lidar and the balloon profile is found in OHP [10,11], and the similar phenomenon in our system. Although these drift is not a limitation for geophysical studies such as waves, mean shear, and etc., it is desirable to make a system with no drift. By replacing the FPI with I_2-vapor cells for frequency locking and discrimination,

#210185 - $15.00 USD Received 18 Apr 2014; revised 24 Jun 2014; accepted 25 Jun 2014; published 8 Jul 2014

one can solve this problem for a system working at 532 nm [16–19]. In the OHP Rayleigh Doppler lidar, their choice is to design a specific instrumentation to change the line of sight very quickly so as to the vertical pointing can be used to eliminate the bias [11]. However, such solutions are not appropriate for our system working at 355 nm, where the telescopes are titled at a fixed angle.

Two sets of experiments are carried out in a laboratory environment to verify the thermal effect and the resulting wind deviations. During the experiments, the FPI and the seeder laser are set in sealed containers, which are temperature controlled with a peltier resistance. The ambient temperature of the FPI are tuned regularly with vibration amplitude of ± 0.3 K and ± 0.05 K, whereas the ambient temperature of the seeder laser keeps constant. The frequency drift of the outgoing laser with respect to the FPI is monitored by a servo loop acting on the FPI tuning control during both experiments. The variations of FPI ambient temperature and the frequency drift related wind deviations are presented in Fig. 9. By FFT (Fast Fourier Transform) analysis, one can clearly see that the wind deviations shows the same periodical oscillation as the temperature in the first case, but no such characteristic feature in the second one. Corresponding vibration amplitude in wind deviation within 5 hours of ± 1.81 m/s and ± 0.5 m/s are obtained.

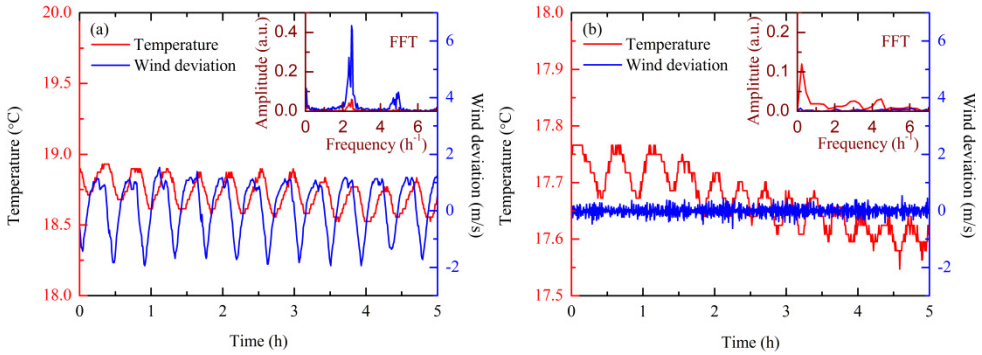

Fig. 9. The variation of FPI temperature and wind deviation with respect to time; in the upper right corner, the result of FFT analysis is present.

Actually, the bias arises mainly from two aspects: one is the frequency drift of the seeder laser and frequency dithering produced during the process of matching the cavity of the low power oscillator to the seed laser frequency; another is the spectral drift of the FPI. Different from the ALOMAR system [18], the seeder laser used in this work is a continuous–wave, single-mode laser with single output at 1064 nm. Fiber coupling of the seeder laser allows its separation from the pulsed oscillator and place in a temperature-controlled chamber. However, the output frequency shows a drift, which directly affects the slave laser wavelength emission at 355 nm. Such a behavior has been reported by McGill et al. with a similar injection-seeded laser [44]. Solution of stabilization is obtained by exactly thermal control of the seeder crystal or with an external stable reference laser operating at a quasi-fixed frequency [45]. In the seeder laser, a cavity is established by two fiber Bragg gratings (FBG) that are fusion spliced to a short piece of Ytterbium-doped fiber. Two temperature effects cause the drift of the seeder output frequency. The first is a wavelength change of the mode selecting narrow band fiber Bragg grating with a frequency tuning coefficient of ~1.5 GHz/K. The second is the wavelength shift of the longitudinal cavity modes of the seeder laser with respect to the center of the spectrally narrow fiber Bragg grating that acts as the seed laser output coupler with a frequency tuning coefficient of ~0.3 GHz/K. Accurate temperature control for the temperature-sensitive optical elements within the seeder ensures consistent performance with minimal operator adjustments. After a warm-time of 30 minutes

#210185 - $15.00 USD Received 18 Apr 2014; revised 24 Jun 2014; accepted 25 Jun 2014; published 8 Jul 2014

to full operating conditions, the frequency stability of 1.6 MHz RMS (root-mean-square) could be realized over 2 minutes with a temperature fluctuation of ± 0.1 K.

Instead of the pressure scanning FPI driven by a stepper motor used in OHP Rayleigh lidar, a cavity scanning one which is piezoelectric-tunable and capacitive-servo-stabilized is utilized in this work. The FPI central wavelengths, given by the cavity spacing, are expected to drift under thermal changes. The FPI has a 56-mm aperture with mean cavity length of 12.5 ± 0.005 mm. The difference between the cavity spacing corresponding to the double-edge channel is 75.44 nm. As the FPI is made of glass-ceramics with high temperature stability, the relative variation of the cavity geometric spacing is given by the thermal dilatation of the order of ± 50 pm/K according to the manufacturer. For each FPI channel, the spectral drift is proportional to the cavity spacing. As the relative difference in cavity spacing among all channels is 6×10^{-6}, it is negligible in this context. The spectral spacing is then a constant value that is independent of possible thermal instabilities or drifts. It follows that the calibration function giving the line position from the response is not affected by thermal instabilities. So the consequence of thermal variations could be considered as an overall drift of the FPI bandpasses with respect to emitted frequency. Theoretically, this drift is given by

$$\Delta v(T) = \frac{5.1GHz}{75.44nm}\Delta l(T), \tag{4}$$

where $\Delta l(T)$ represents the cavity length variation introduced by temperature fluctuation. Provided that the maxima temperature variation is ± 0.1 K and take the drift of the seeder laser into account, an equivalent horizontal wind velocity bias of ± 0.6 m/s for our system and ± 14 m/s for the OHP system [11] is obtained, which is well coincident with the experimental results.

5. Wind and temperature observations

Wind and temperature observation is performed in Delhi (37.371° N, 97.374° E), northwest of China, throughout December, 2013. Radiosonde data are available to validate the lidar performance including horizontal wind and temperature profile in this area. Figure 10(a) shows the mobile Rayleigh Doppler as a payload of the support vehicles. The whole system is integrated on two trucks: the subsystem pointing to the zenith is loaded on the first car and the two others pointing to the north and east are separately loaded on the behind one. The three LOS wind profiles are combined to determine the wind velocity and direction simultaneously. As an necessary input parameter, the temperature profile used in this work is the CIRA (COSPAR International Reference Atmosphere) 1986 model, an empirical model of the upper atmosphere which takes the seasonal variation into accounts, when Lidar data is inaccessible at high altitude (>30 km). An example of typical raw data in the experiment is represented in Fig. 10(b). In order to reduce the statistical standard error of measurement, a long accumulating time of half an hour is executed for each profile, and the available spatial resolution is sacrificed from 200 m (below 40 km) to 1 km (above 40 km). For wind measurement, assuming the photon nosies of the photon counting detectors are uncorrelated and follow Possion statics, the statistical standard error can be estimated with the signal to noise ratio (SNR), which is inversely proportional to the square root of photon counts on the detector. Figure 10(b) reveals that the dark counts of the detectors and background noise is negligible in the altitude range from 90 km to 100 km and therefore narrow bandpass interference filter is unnecessary in the receiver except for daytime operating.

#210185 - $15.00 USD Received 18 Apr 2014; revised 24 Jun 2014; accepted 25 Jun 2014; published 8 Jul 2014

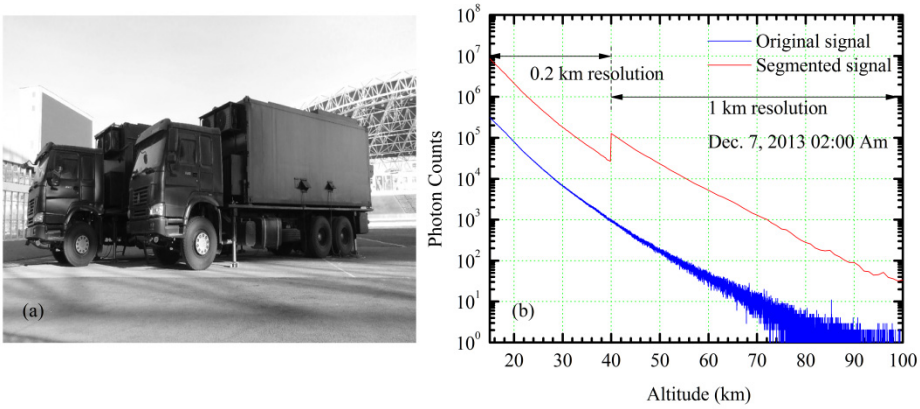

Fig. 10. (a) The USTC Rayleigh Doppler lidar in experiment. (b) Profiles of backscattered signals at 02:00 Am, Dec. 7, 2013. The height resolution is changed from 0.2 km to 1 km at 40 km altitude.

In order to validate the performance of the Rayleigh Doppler lidar, comparison of wind and temperature measurements from the lidar, ECMWF analysis, CIRA model and radiosonde is made in every morning and nightfall throughout December, if weather condition permits lidar operation. A typical result of temperature observations performed at local time (LT) 21:00 on 21 December 2013 is shown in Fig. 11(a). The data is smoothed by a 2 km running mean filter. We find the CIRA model, radiosonde and lidar measurement show good agreement in the altitude range from about 27 km to 45 km. However, the retrieved temperature at altitude below 27 km is biased, as there is no energy monitor channel for numerical iteration to remove the aerosol contribution. This is confirmed by using Klett-Fernald algorithm to retrieve the lidar backscatter ratio, defined as $R = (\beta_a + \beta_m)/\beta_m$. Here β_a and β_m are the backscatter coefficients for aerosols and molecules, respectively. One can see from Fig. 11(b) that the top of the aerosol layer is near 27 km, the same altitude where the retrieved temperature is biased. The bulge been appears in the altitude range from 22 to 27 km may be caused by high-altitude cloud. At altitude above 35 km where radiosonde data is not available, large difference between the ECMWF analyses and lidar measurement occurred in this case, whereas the CIRA model agreed well with lidar measurement. Actually, large difference between lidar and the ECMWF analyses have been discovered and reported by our group in 2012 [23] and by ALOMAR in 2000 [18]. Deficiencies of the ECMWF analysis in producing accurate stratosphere temperature and related real horizontal winds have been recognized earlier when compared with balloon data [46]. Nevertheless, such accuracy is adequate for wind determination, as for typical wind velocity of 50 m/s at this altitude, a temperature error of 10 K introduced wind velocity deviation is merely 0.7 m/s or so. The vertical wind profiles are constant with the altitude and shows no extreme values at 48 km altitude where we observed the maximum temperature, as shown in Fig. 11(c). The resulting nearly zero vertical wind demonstrates that the temperature effect which causes Doppler broadening is correctly treated in the wind retrieval.

#210185 - $15.00 USD Received 18 Apr 2014; revised 24 Jun 2014; accepted 25 Jun 2014; published 8 Jul 2014

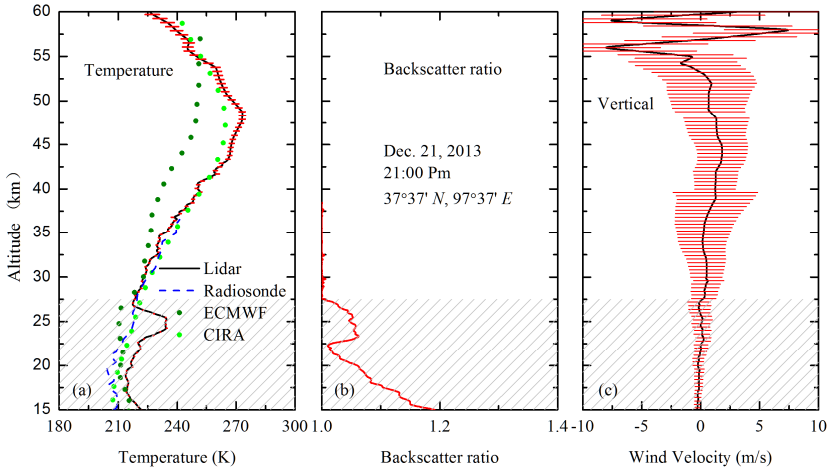

Fig. 11. Lidar backscatter ratio, temperature and vertical wind measured by the Rayleigh Doppler lidar (solid line with error bars) on 21 December 2013. The temperature measurement is compared with ECMWF (olive plots), CIRA model (green plots), and radiosonde measurement (blue dashed line). The sparse-line area indicates altitudes with aerosol contribution as measured by the lidar.

In Fig. 12, two sets of wind profiles from lidar measurement, ECMWF analysis, and radiosonde sounding have been plotted together. As there is no description of horizontal winds in the CIRA model, it will not be presented in the following comparison. Wind measured by Rayleigh Doppler lidar is plotted with error bars, which includes the calibration uncertainty, temperature deviation and statistical standard error. The temperature deviation is expected to be about ± 4 K at 60 km altitude, which will cause an error of about ± 0.5 m/s according to the magnitude of wind velocity. As shown, there is no systematic difference in both wind velocities and wind directions between lidar and radiosonde even if at the aerosol loaded altitudes, which demonstrates our solution that makes wind measurement insensitive to Mie contribution is effective. The vertical structure of wind direction observed by the lidar is similar to that given by the ECMWF analysis. However, it is noteworthy that we find large difference in wind velocity especially at altitudes below 25 km and above 40 km between them. The reflection point in wind profile observed by lidar is about 5 km lower than that given by ECMWF analysis in the tropopause region. In this experiment, the velocity and direction measurement uncertainties are 7.6 m/s and 13.6°at 60 km altitude, respectively.

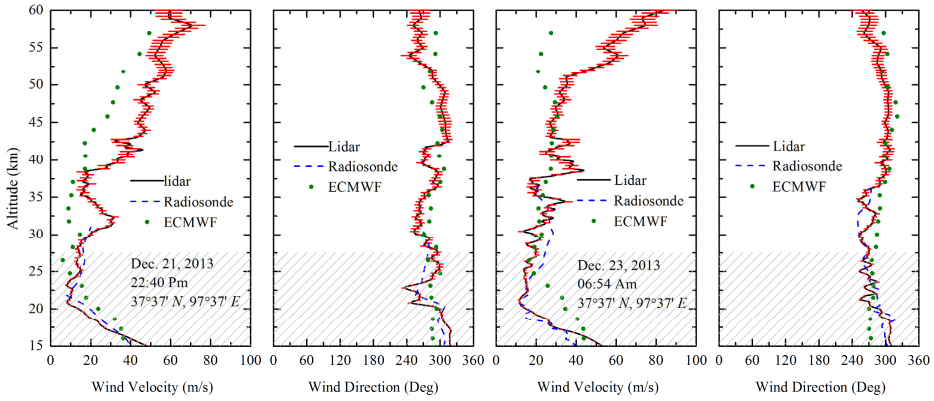

Fig. 12. Profiles of horizontal wind velocity and direction measured by the Rayleigh Doppler lidar compared with data from radiosonde at LT 22:40, December 21 and at LT 06:54, December 23. The upper altitudes of aerosol loaded region on two days is 27.5 km, as is the sparse-line area presented in this figure. This result is 6000 shots accumulated.

#210185 - $15.00 USD Received 18 Apr 2014; revised 24 Jun 2014; accepted 25 Jun 2014; published 8 Jul 2014

Continuous wind field observation is performed throughout December, 2013 and semi-continuous wind field of 16 nights are presented. The dynamic structure of mid-altitude atmosphere and its evolution are clearly shown in Fig. 13. Similar to the result observed by our prototype lidar in September and October 2011, the stable quasi-zero wind layer appears again with mean wind velocity of about 4~6 m/s from 22 to 27 km altitudes. A minor difference between them is the center altitude changed from 20 km to 25 km. While for wind direction, the consistent winter westerlies at this latitude are the most prominent features. The stratospheric quasi-zero wind layer was firstly proposed by Belmont *et al.* and thought to be closely related to the combined effect of midlatitude circulation and Quasi-Biennial Oscillation (QBO) [47]. Later researches reveal such a feature may be caused by the reversal of meridional temperature gradient in lower stratosphere. However, further study is required to explain this interesting phenomenon by the help of ancillary data in the near future.

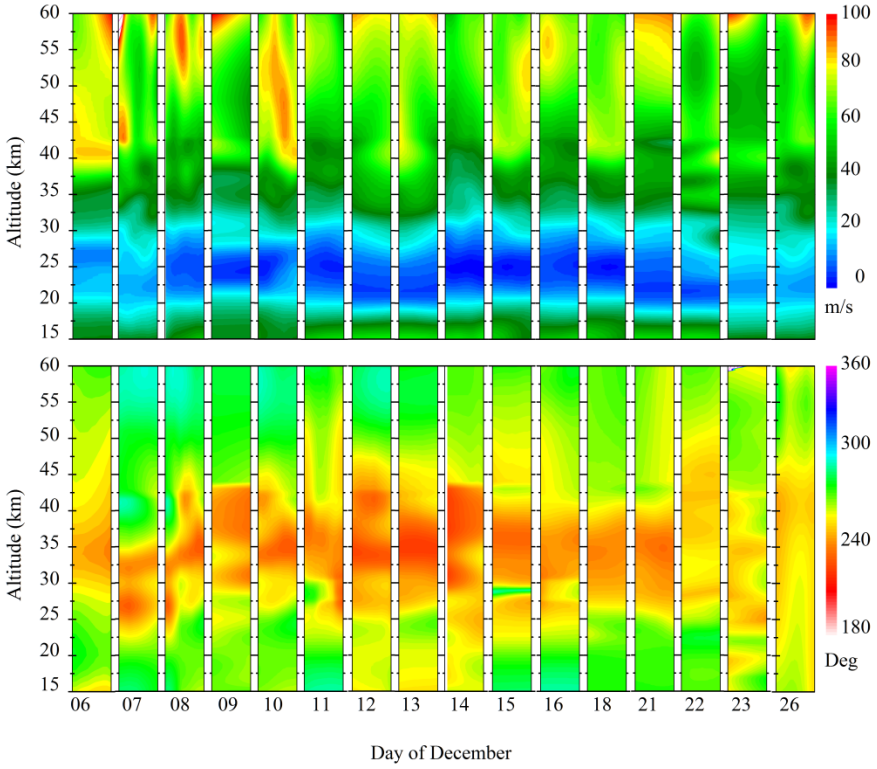

Fig. 13. Time-altitude cross section of semi-continuous horizontal wind field observed by mobile Rayleigh Doppler lidar in December 2013. For every night, 6 hours' measurement is presented in this figure from LT 00:00 to 06:00 with time resolution of half an hour. The maximum velocity and direction error in this experiment are estimated to be 9.2 m/s and 14.3°, respectively.

6. Conclusion and future research

A mobile Rayleigh Doppler lidar for wind and temperature measurement in the stratosphere and lower mesosphere from 15 to 60 km is successfully implemented and demonstrated. The new generation lidar enhanced the performance of the prototype one and can realize simultaneous wind and temperature observation. Currently, the accuracy of the wind measurement is dominated by the random noise of the atmospheric signal. An accumulating time of half an hour is executed to reduce the statistical standard error with spatial resolution changed from 0.2 km (below 40 km) to 1 km (above 40 km). In the comparison experiments,

#210185 - $15.00 USD Received 18 Apr 2014; revised 24 Jun 2014; accepted 25 Jun 2014; published 8 Jul 2014

wind measured from lidar, ECMWF analysis, CIRA model and radiosondes were in good agreement in the altitude from 15 to 35 km. Continuous measurement of horizontal wind was performed, demonstrating the stability and robustness of this system.

For future research, long-term and simultaneous monitor of mid-atmosphere will be performed to reveal the dynamic structure and its seasonal variation. Studies of various scales of dynamics, such as gravity waves and sharp wind shear encountered at the upper stratosphere will be paid special attention. Now in USTC, there exist Mie Doppler lidar, Rayleigh Doppler lidar and Sodium lidar for wind and temperature measurement. Combination of them achieve a coverage from ground to 105 km with the only gap between 60 km and 80 km [23, 26, 48]. Therefore, to fulfill the gap of combined observation from troposphere to lower thermosphere would be the goal of our next generation lidar in the near future.

Acknowledgments

We appreciate greatly the efforts of the reviewers and their constructive comments and gratefully acknowledge the European Centre for Medium-Range Weather Forecasts (ECMWF) for providing the wind and temperature data. This work was supported by CAS (Chinese Academy of Sciences) Special Grant for Postgraduate Research-Innovation and Practice and the National Natural Science Foundation of China (41174130, 41174131 and 41227804).

#210185 - $15.00 USD Received 18 Apr 2014; revised 24 Jun 2014; accepted 25 Jun 2014; published 8 Jul 2014